





SolMech 2024

Assessment of GFRP Reinforcement Bars Condition Based on Elastic Wave Propagation

Anna RZEPKA*, Dominika ZIAJA, Michał JUREK,
Agnieszka WIATER

*Faculty of Civil and Environmental Engineering and Architecture
Rzeszow University of Technology*

Rzeszów, Poland; e-mails: dziaja@prz.edu.pl, mjurek@prz.edu.pl, wiaater@prz.edu.pl

*Corresponding Author e-mail: a.rzepka1@prz.edu.pl

New technologies in construction constitute a crucial element of effective development. Contemporary trends have led to increasing interest in composite materials, mainly due to their unique properties. The flexibility in shaping composite materials enables the production of reinforcing bars, providing a viable alternative to the widely used steel bars. The implementation of innovative solutions necessitates monitoring the performance of structures. Using information on the propagation of elastic waves is one of the non-destructive testing (NDT) methods for observing the construction behavior. An effort to employ this technique in the assessment of the anchoring condition and stress evaluation in glass fiber-reinforced polymer (GFRP) bars is presented in this study. During laboratory testing, samples of ribbed bars with diameters of $\phi 6$ mm, $\phi 10$ mm, and $\phi 16$ mm were used (a total of 20 bars). Measurements were performed using laser Doppler vibrometry and piezoelectric transducers (PZT). Elastic waves were excited using a PZT sensor attached to one end of the bar, and the wave propagation was recorded in three ways: using a PZT sensor at the opposite end of the bar, using LDV at the opposite end, and on the sidewall. The research included samples of bars without anchorage, bars with anchorages (used for placement in a strength-testing machine), and specimens subjected to tensile testing (according to ISO 10406-1:2015). The collected signals were compared in both the time and frequency domains, considering variations in wave propagation due to different diameters, anchoring methods, and stress states. Based on the obtained results, it can be concluded that the analysis of the elastic wave propagation holds potential for assessing the condition of GFRP reinforcing bars.

Keywords: composite reinforcement; GFRP bars; elastic wave; non-destructive testing.



Copyright © 2025 The Author(s).
Published by IPPT PAN. This work is licensed under the Creative Commons Attribution License
CC BY 4.0 (<https://creativecommons.org/licenses/by/4.0/>).

1. INTRODUCTION

The dynamically evolving construction industry requires the search for innovative and technologically advanced materials. Composites (materials produced by combining at least two components) can be classified as materials of the future, gaining increasing significance due to a range of advantageous properties

(such as high tensile strength, low self-weight, and good corrosion resistance) [1, 2]. Glass fiber-reinforced polymer composites belong to the broader category of fiber-reinforced composites. The flexibility in shaping these materials enables the production of reinforcement bars, which serve as alternatives to conventional steel reinforcement bars [3]. Modern engineering demonstrates growing interest in reinforcement bars [4], particularly in the bridge industry, where they are used as elements of deck reinforcement. Composite reinforcement bars are used in both new engineering structures and the modernization of existing ones (such as bridge widening or deck replacement) [5, 6]. Composites, a relatively new alternative to traditional materials, require monitoring of the structural condition, which can be effectively achieved through non-destructive testing methods [7]. Among the numerous NDT methods, elastic wave measurement and analysis are commonly used.

Researchers widely discuss the propagation of elastic waves in bars as a key aspect of studying mechanical properties and response to dynamic loads. This phenomenon is analyzed using both experimental methods and numerical simulations. With laser Doppler vibrometers and piezoelectric transducers, waves passing through the bar can be precisely recorded and analyzed [8, 9]. ZHANG *et al.* [10] investigated waves in elastic rods under axial constant velocity loading. They demonstrated that axial waves in elastic rods influence dynamic stability and can potentially cause rapid buckling. In turn, ZHANG and WANG [11] employed artificial neural networks to predict the propagation of elastic waves in composites. They demonstrate the relationship between the material's microstructure and wave propagation. RIGBY *et al.* [12] examined the dispersion problem in the Hopkinson pressure bar, analyzing it in the context of the Pochhammer–Chree equation, which was originally described in [13].

Scientists are increasingly analyzing the behavior of composite bars in building structures. HUANG *et al.* [14] and CHEN *et al.* [15] investigated the performance of connections between composite steel and fiberglass bars and concrete. They analyzed the adhesion forces between the materials as well as mechanical properties such as tensile strength and corrosion resistance. In turn, RUCKA *et al.* [16] discussed the results of experiments and proposed a data analysis algorithm that accurately assesses the quality of reinforcement bar anchorage based on elastic waves. The topic of composite reinforcement bar anchorage was also discussed in [17], where the authors investigated the effect of the anchorage length of GFRP reinforcement bars in concrete columns. Strength tests carried out on the anchored bars demonstrated that appropriate anchorage length significantly affects the efficiency of force transfer and the structural strength.

This article discusses the potential for assessing the condition of GFRP reinforcement bars based on the propagation of elastic waves. The authors investigated the effect of anchorage on elastic wave propagation and examined

the influence of the applied force on the bars. Additionally, the failure process of the bars was analyzed, with an attempt to identify common damage features based on the elastic wave propagation. The research on GFRP bars is motivated by the development of composite bar applications as an alternative reinforcement in civil engineering structures (CES). These reinforcement bars are primarily located in tensile zones within such structures and are responsible for transferring tensile forces. The authors explore the application of elastic wave propagation phenomenon to monitor the condition of CES reinforced with GFRP, making it crucial to determine the influences of strain state on wave propagation in bars made from this material. To ensure objectivity, the influence of varied diameters and anchorage conditions was also considered.

2. MATERIALS AND METHODS

Laboratory tests were conducted on composite ribbed bars made of glass fiber. The bars varied in diameter, total length, and anchorage zone length. Table 1 presents detailed data on the tested bars [18]. In total, 20 bars were examined: 5 with a diameter of 6 mm, 10 with a diameter of 10 mm, and 5 with a diameter of 16 mm (Fig. 1). Each sample was assigned an alphanumeric

TABLE 1. GFRP bar test details.

Sample label	Resin and fiber content by weight	Material density [kg/m ³]	Modulus of elasticity [GPa]	Bar size [mm]	Bar length [mm]	Length between anchorages [mm]
P0601a-P0605a	epoxy 75–80%	2075	50 ± 5	6	1028–1036	380
P1001b-P1005b P1006c-P1010c				10	1028–1039	400
P1601c-P1605c				16	1347–1352	550

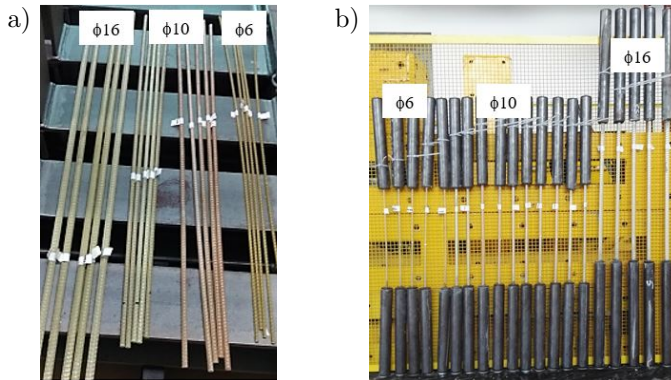


FIG. 1. GFRP bars: a) unanchored, b) anchored.

code (for example, “P0601” indicates a bar with a 6 mm diameter, where “01” represents the first sample). The additional letters “a”, “b”, and “c” refer to different production batches (variations in rods’ color shown in Fig. 1a may indicate different resin modifications used in the manufacturing process; however, the declared strength parameters remained unchanged).

Laser vibrometry (Polytec Scanning Vibrometer PSV-400-3D) and piezoelectric transducers ($5 \times 5 \times 2$ mm CMAP7 transducers by Noliac, attached using wax and quick-drying glue) were used to investigate elastic wave propagation. The GFRP bars tests involved analyzing the rods in two states: unanchored (Fig. 1a) and anchored with a steel pipe filled with concrete (Fig. 1b). The examination was conducted in four steps (shown schematically in Fig. 2):

- unanchored bars (Fig. 2a) – secured with fastening cables on a supporting frame; wave measurement with LDV on the sidewall and in the front; no loads applied,
- anchored bars (Fig. 2b) – laid on the supporting frame; wave measurement with LDV on the sidewall and in the front; no loads applied,
- anchored bars (Fig. 2c) – laid on the supporting frame; wave measurement with by PZT sensor at the front; no loads applied,
- standard tensile test (Fig. 2d) – anchored specimens mounted in a standard testing machine; PZT measurements at the front; LDV measurement on the sidewall; load gradually increased.

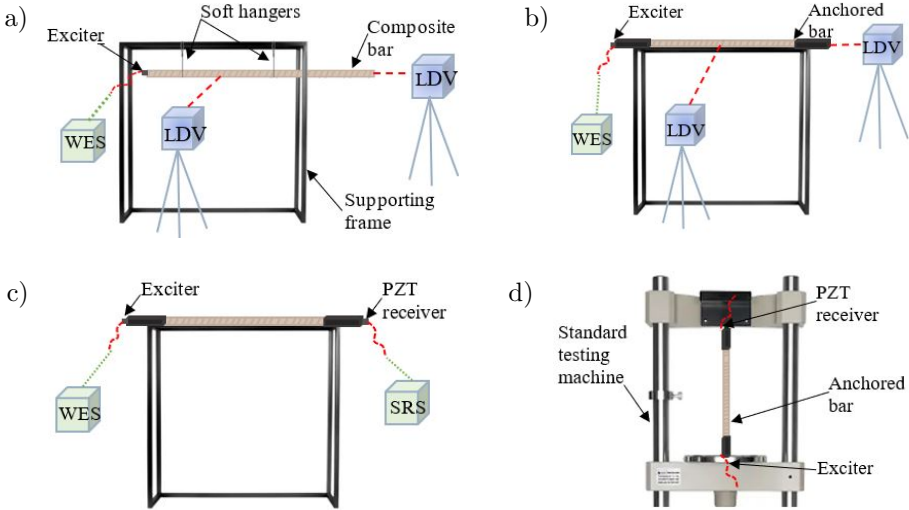


FIG. 2. Measurement setup for: a) unanchored bars, b) anchored bars, c) anchored bars with PZT transducers using LDV, d) anchored bars in the standard testing machine; WES – wave excitation set (wave generator, amplifier, exciter), SRS – signal recording set (signal pre-amplifier, oscilloscope).

In Fig. 2, the WES box represents the wave excitation set, which includes a wave generator, amplifier, and exciter. The SRS box depicts the signal recording set, which consists of a signal pre-amplifier (AEP5x5-V2 Vallen Systeme GmbH) and a 4-channel digital oscilloscope (LeCroy WaveRunner 104 Mxi). The laser Doppler vibrometer corresponds to the LDV boxes.

Regardless of the task, the wave was excited with PZT sensor glued to one end of the bar. Waves were generated using a 2.5 sine wave packet at a frequency of 10 kHz and amplitude of 8 Vpp, amplified 20 times. The measurement point on the sidewall was located 50 cm from the actuator, while the measurement point at the front of the bar was opposite the exciter. Tests on unanchored bars included analyzing the effects of sensor glueing, bar length, diameter, and material. At this stage, five rods with a diameter of 6 mm and ten rods with a diameter of 10 mm were analyzed. All rods were selected for the series of tests on anchored rods. In this stage, the effects of rod length and diameter were analyzed. The change in wave propagation due to anchoring was also investigated. The final stage of the anchored bar tests focused on analyzing the influence of applied forces and observing the nature of breakage. The impact of the applied force on wave propagation was examined by measuring the waves at the ends and sidewalls of rods with diameters of 10 mm and 16 mm (five rods of each diameter). Due to the small diameter of the rod and difficulty in precisely locating a measurement point on a non-curved fragment, 6 mm rods were excluded from this stage. A tensile test was conducted using a testing machine in accordance with ISO 10406-1:2015, which specifies test methods for fiber-reinforced polymer (FRP) reinforcement of concrete, including FRP bars and grids. The results of this test are detailed in [19]. The bars were loaded in 10 kN increments, with 10 mm diameter rods tested up to 70 kN and 16 mm diameter rods up to 150 kN. After each increment, a stabilization period followed, during which elastic wave propagation through the bar was recorded. This process was then repeated with each subsequent load step. Figure 3 shows results obtained from the testing machine, with an example for sample P1006.

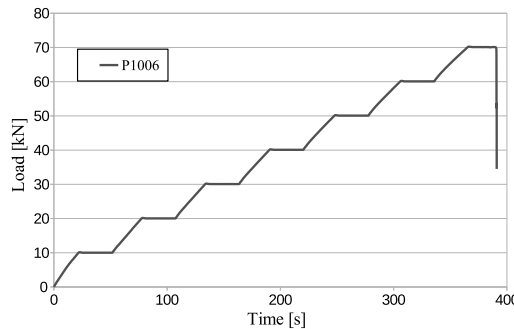


FIG. 3. Time-load curve for sample P1006.

3. TEST RESULTS AND DISCUSSION

3.1. Results for unanchored bars

3.1.1. The effect of actuator attachment. The collected signals were analyzed in both the time and frequency domains. Based on the frequency domain signal analysis, a bandpass filter was selected to reduce measurement noise, retaining frequencies in the range of 20–33 kHz (corresponding to the effective frequency of the wave excited by 2.5 cycles of sine wave at 10 kHz, i.e., 25 kHz). Figures 4 and 5 show example results of the filtered signal for an unanchored rod with a diameter of 6 mm, recorded respectively from the front and the side-wall. Figures 4a and 5a show the original signal, Figs. 4b and 5b presents the signals transformed into the frequency domain, both before filtering (blue) and after filtering (red), while Figs. 4c and 5c compare the original signals (blue) with the filtered signals (red) in the narrowed time interval. Comparing Figs. 4 and 5, differences in the number of cycles and amplitude due to different measurement locations can be seen. Furthermore, Figs. 4c and 5c show differences in how wave propagates depending on the measurement location. Similar trends were observed for rods with a diameter of 10 mm.

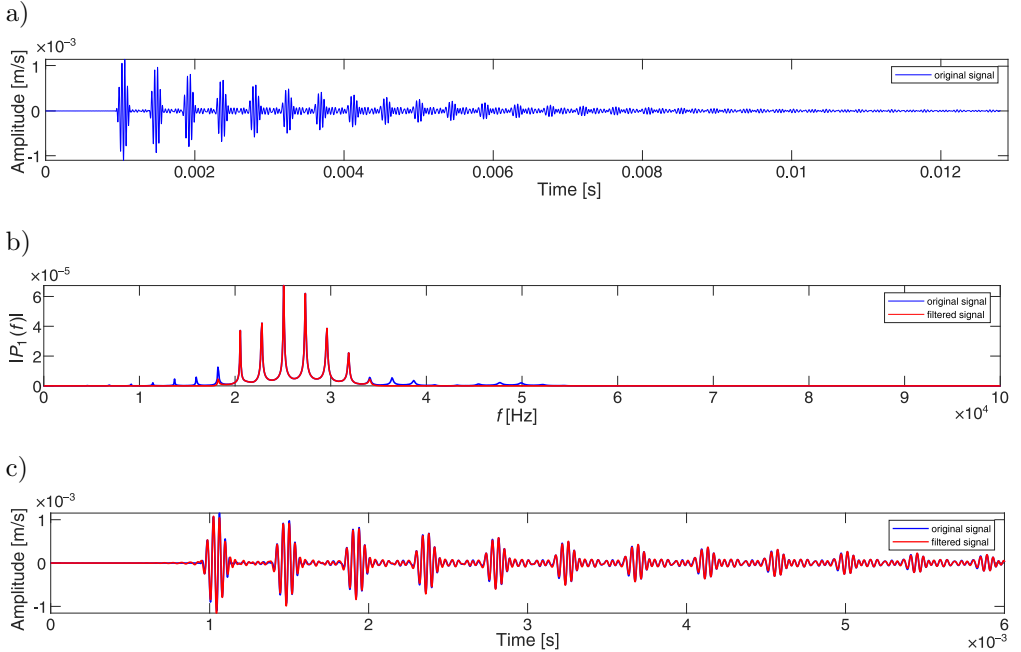


FIG. 4. Exemplary elastic wave measurement registered using the LDV technique for an unanchored rod with 6 mm diameter: a) the original signal registered from the front, b) single-sided spectrum of the original and filtered signals in the range of 0–100 kHz, c) comparison of original and filtered signals in a narrowed time interval.

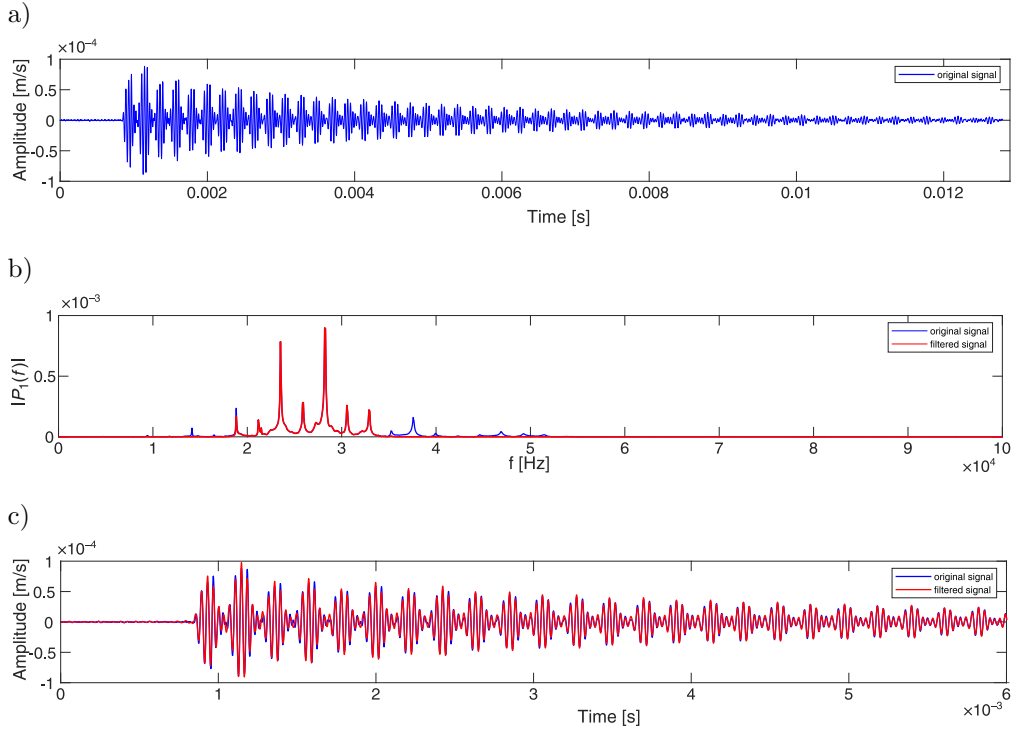


FIG. 5. Exemplary elastic wave measurement registered using the LDV technique for an unanchored rod with 6 mm diameter: a) original signal registered on the sidewall, b) single-sided spectrum of the original and filtered signals in the range of 0–100 kHz, c) comparison of original and filtered signals in a narrowed time interval.

Between each pair of tests, the sensor was removed and reattached to the bar using wax. Figure 6 presents an example of three measurements taken from a bar sample with a diameter of 6 mm, showing the filtered signal measured from the front. By comparing Figs. 6a, 6b, and 6c, differences in the number of clearly visible cycles across the measurements can be observed (highlighted in the red-marked area). Additionally, amplitude values vary among Figs. 6a–6c. The first three cycles are highlighted in green: the first cycle corresponds to the wave reaching the opposite end of the rod, while the second and third cycles represent successive reflections – the wave returns to the excitation end, reflects off the edge, and then again returns to the measurement point. Therefore, the distance between consecutive cycles reflects the time interval required for the wave to travel twice the length of the rod. These differences may arise from variations in the length of the bar as well as from the attachment of the exciter (despite using the same adhesive and excitation source). The authors of [20] discuss this issue and indicate that changes in the method of actuator attachment,

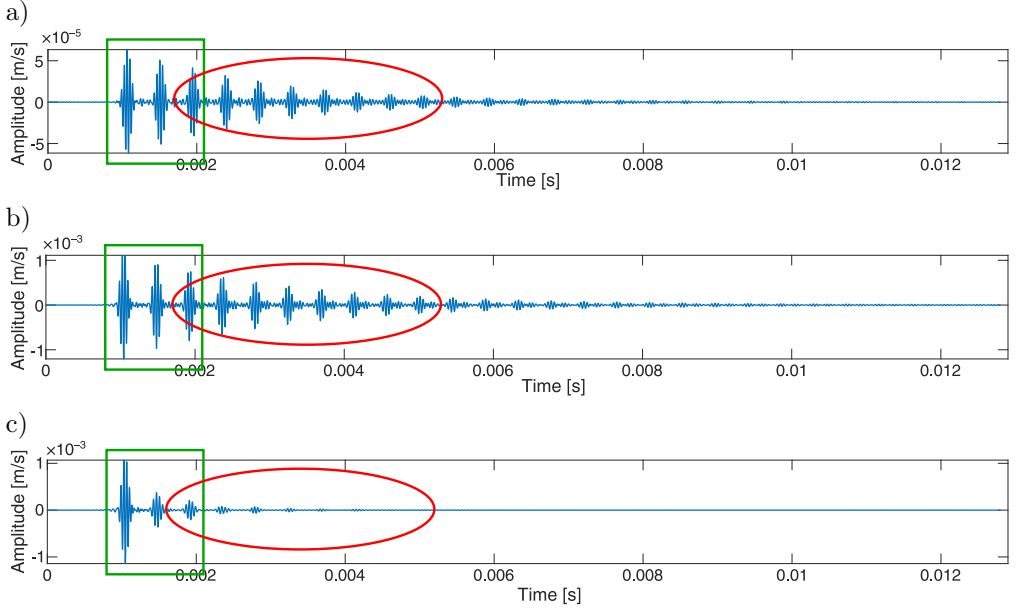


FIG. 6. Wave propagation measured from the front of the unanchored bar for sample P0603: a) first measurement, b) second measurement, c) third measurement.

such as those depending on the precision of application or adhesive distribution, impact the generated wave.

Figure 7a shows the wave propagation for the unanchored rod with a diameter of 10 mm measured from the front, while Fig. 7b shows the measurement taken on the sidewall. Figure 7a demonstrates a more significant number of wave packets compared to Fig. 6. The excitation parameters were consistent for rods

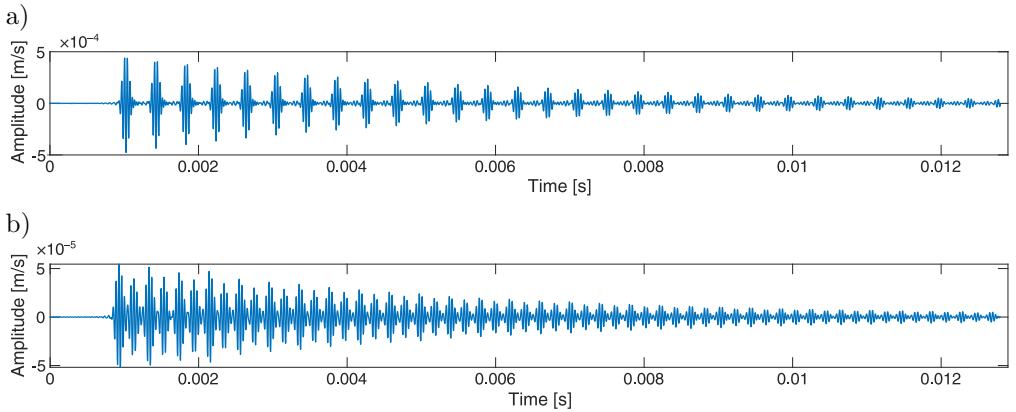


FIG. 7. Wave propagation measured of the unanchored bar for sample P1006: a) from the front, b) on the sidewall.

of different diameters, and the signal recorded at the end of the measurement period is of higher quality (with distinct wave packets visible). A larger rod diameter appears to facilitate easier wave propagation with lower losses. Analysis of the remaining data revealed that similar differences are also evident in other samples.

The differences observed in multiple measurements of the same sample arise because it is not possible to attach the sensor to the sample in the same position after it has been removed. The attachment of the sensor is not repeatable due to variations in adhesive thickness and potential shifts of the actuator relative to the bar axis, even with precise attachment. For bars with a diameter of 6 mm, greater variations in wave propagation between measurements are observed compared to bars with diameters of 10 mm and 16 mm. This may be due to the ratio of the actuator size to the rod diameter (as the same sensor was used regardless of rod size). Changes in attachment affect both the wave measured along the rod's axis and the one measured on the sidewall. The differences in waves recorded on the sidewall appear to be greater than those recorded from the front. This is possible because the laser does not always precisely target the same point on different specimens. As a result, it is easier to hit a point on the flat surface of the rod (from the front) than on its curved part (the ribbed sidewall).

When comparing signals recorded for the 6 mm diameter samples (Fig. 6) and the 10 mm diameter samples (Fig. 7), a significant difference (by an order of magnitude) in amplitude is observed despite identical excitation conditions for both types of samples. The same trend was consistent across other the remaining samples. Due to amplitude variations in signals recorded for the same sample after detaching and reattaching the actuator (see Figs. 6a and 6b), the collected time-series data were normalized to the range $\langle -1, 1 \rangle$ for further analysis.

3.1.2. Influence of geometric and material parameters of bars. Wave propagation in bars of different lengths was investigated experimentally. For the analysis, the shortest and longest specimens from each type were selected (all rods were produced within the same manufacturing batch). The following samples were chosen:

- $\phi 6$ mm: P0602: length 1028 mm and P0603: length 1036 mm,
- $\phi 10$ mm: P1006: length 1029 mm and P1007: length 1039 mm.

In Fig. 8, the waveforms measured from the front of two 6 mm samples, differing by 8 mm in length (P0602 and P0603) are presented. Figure 8a shows the waveforms in a narrowed time interval, while Fig. 8b presents a close-up view of the region with the highest amplitude, highlighted by a green rectangle. No significant differences between the signals for the two bars in the initial

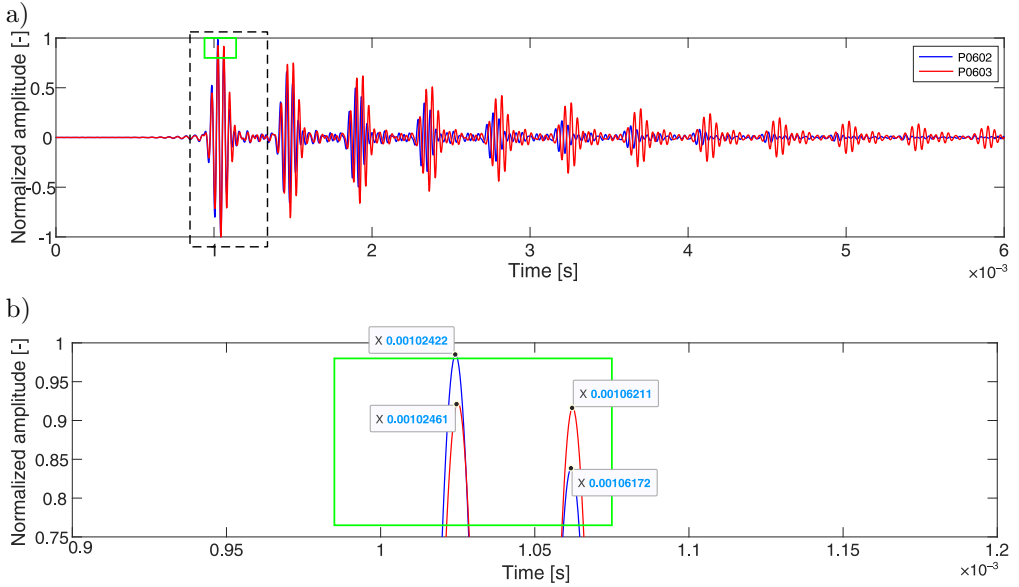


FIG. 8. Wave propagation from the front for 6 mm diameter unanchored bars: a) signal in the narrowed time interval, b) close-up view of the region of the highest amplitudes.

propagation phase were observed. In the case of the first wave cycle (marked with a black dashed rectangle in Fig. 8a), the waves overlap each other, and the phase difference is difficult to detect. The zoomed-in view of the region with the highest amplitude (Fig. 8b) reveals only a slight phase difference between the waves for both samples.

Additionally, the exact values of the time shift for the highest amplitudes in Fig. 8b are marked. The phase shift between the two wave segments is less than 0.1%. The influence of the bar length difference on elastic wave propagation becomes more noticeable with successive reflections of the wave from the bar ends. Similar effects were also observed for bars with a diameter of 10 mm. In this case, the difference in the time shift in the region of the highest amplitudes is about 0.5%.

In summary, the impact of rod length differences on the time corresponding to the peak wave amplitude after the first (or second) pass is minimal. However, this impact becomes more pronounced with subsequent waves traveling through the rod. Thus, the analysis could be limited to a narrower time interval of $(0.0007 \text{ s}, 0.0017 \text{ s})$, corresponding to 2.5 wave cycles for unanchored bars.

Rods with different diameters and slightly varying lengths were selected for comparison. The selected samples are P0602 (1028 mm) and P1006 (1029 mm). Figure 9 presents the waveforms for rods of different diameters in a narrowed

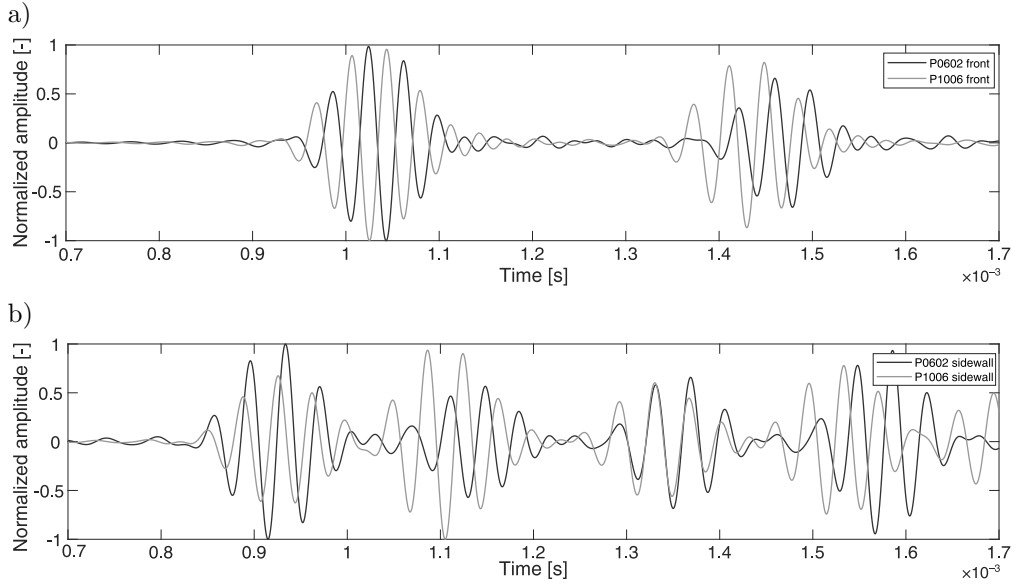


FIG. 9. Wave propagation in unanchored bars of different diameters:
a) wave measured from the front, b) wave measured on the sidewall.

time interval. Figure 9a shows the wave recorded from the front, while Fig. 9b shows the wave recorded from the sidewall. Comparing Figs. 9a and 9b, it can be observed that the wave's behavior and characteristics vary significantly depending on the measurement location. In Fig. 9a, the rod with the larger diameter exhibits more pronounced signal attenuation, particularly in the regions between consecutive wave packets. The phase shifts of approximately 2–3% observed in Fig. 9 may be attributed to differences in wave propagation speed in the medium. As shown in [19], the rod with the larger diameter of 10 mm has a different Young's modulus, which influences the phase velocity (according to Eq. (3.2)) compared to the rod with the smaller diameter of 6 mm.

The next stage of the analysis involved checking whether differences in resin modification during the manufacturing process affect the propagation of elastic waves. The selected bars have the same diameter and length. Sample codes are P1002b and P1007c. Figure 10a shows the wave measured from the front, while Fig. 10b shows the wave measured from the sidewall. In Fig. 10, one can observe that despite originating from different production batches, the wave characteristics for both rods are very similar. Slight phase shifts may result from differences in the rods' density, Poisson's ratio, or Young's modulus, which can influence variations in the wave propagation speed. Even minor changes in material composition can lead to small but noticeable differences in elastic wave propagation, as shown in Fig. 10.

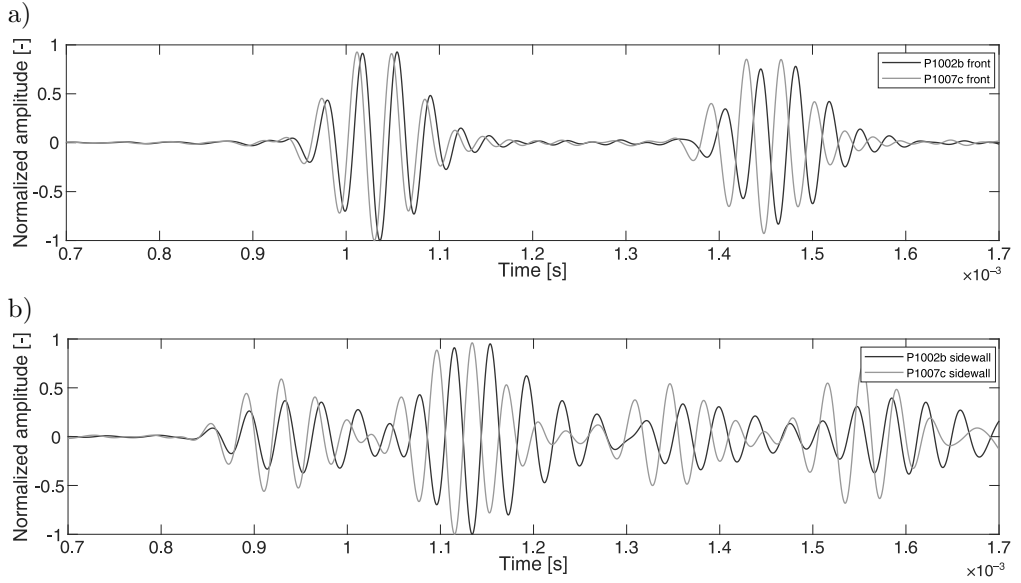


FIG. 10. Wave propagation in 10 mm diameter bars from different production batches: a) wave measured on the front, b) wave measured from the sidewall.

Wave speed calculations were conducted to gain a more detailed understanding of how bar length and bar diameter affect wave propagation. Initially, the velocity was estimated individually for each bar using the formula:

$$(3.1) \quad v = \frac{X}{t} \quad [\text{m/s}] \quad [21],$$

where v denotes the wave velocity, X is the bar length, and t is the time. The time value used to calculate the wave speed was obtained from signal analysis (measured between the peaks of adjacent signal packets). The results are provided in Table 2.

TABLE 2. Comparison of elastic wave velocity, determined experimentally, and phase velocity calculated by solving the Pochhammer–Chree equation (corresponding to the excitation frequency $f = 25$ kHz), for $E = 50 \pm 5$ GPa.

Sample label	Wave velocity [m/s]	
	v	C_p
P0602	4720	4924–5443
P0603	4715	
P1002	4867	4922–5440
P1006	5095	
P1007	4976	

The elastic wave propagation in bars is described by the Pochhammer–Chree equation [12, 13]:

$$(3.2) \quad (x - 1)^2 \Phi(ha) - (\beta x - 1)[x - \Phi(ka)] = 0 \quad [12, 22],$$

where $x = (C_p/C_0)^2(1 + \nu)$, $\beta = (1 - 2\nu)(1 - \nu)$, $h = \gamma\sqrt{(\beta x - 1)}$, $k = \gamma\sqrt{(2x - 1)}$, $\Phi(y) = yJ_0(y)/J_1(y)$, $\gamma = 2\pi/L$, a is the bar radius, C_0 the longitudinal wave velocity, C_p – the phase velocity, L – the wavelength, ν – Poisson’s ratio, and $J_n(y)$ – is a Bessel function of the first kind of order n .

By numerically solving Eq. (3.2) using the material parameters presented in Table 1 (density and modulus of elasticity) and assuming a Poisson’s ratio $\nu = 0.20$ (assumed based on [1, 23]), the phase velocity was calculated. The results for the excitation frequency of 25 kHz, which corresponds to the frequency used in the experiments, are shown in Table 2. It should be noted that the material properties significantly influence wave velocity, and these properties were not precisely known for the analyzed bars. Table 2 shows the influence of varying the modulus of elasticity (with the lower bound in the third column set at $E = 45$ GPa, and the upper one at $E = 55$ GPa). The influence of density variations and Poisson’s ratio was not analyzed in this study. The differences in theoretically calculated phase velocity resulting from changes in bar diameter (in the analyzed range) appear to be insignificant compared to the variability resulting from material properties. Despite that, a difference between wave velocities for bars of different diameters is visible in experimental data. This observation is consistent, as mentioned earlier, with findings reported in [19]. Moreover, differences in velocity (on the order of approximately 2%) were observed in rods with the same diameter and length but from different production batches (P1002 and P1007).

To sum up, tracking changes in recorded elastic wave signals, such as variations in their propagation, can provide insights into the material and geometric parameters of the examined object.

3.2. Results for anchored bars

3.2.1. Influence of the anchoring effect of bars. The next stage involved assessing the impact of bar anchorage. Figure 11 presents the time signals for unanchored (blue signal) and anchored (red signal) bars. Figure 11a shows the signal recorded from the front, while Fig. 11b shows the signal recorded on the sidewall.

The first noticeable difference is the variation in amplitudes. This may be due to the fact that the exciter on the unanchored bars was attached with wax, while on the anchored bars it was attached with quick-dry glue. As mentioned before, the method of exciter attachment is crucial [19]. The adhesive was changed during the experiments to prevent the exciter from detaching during testing of

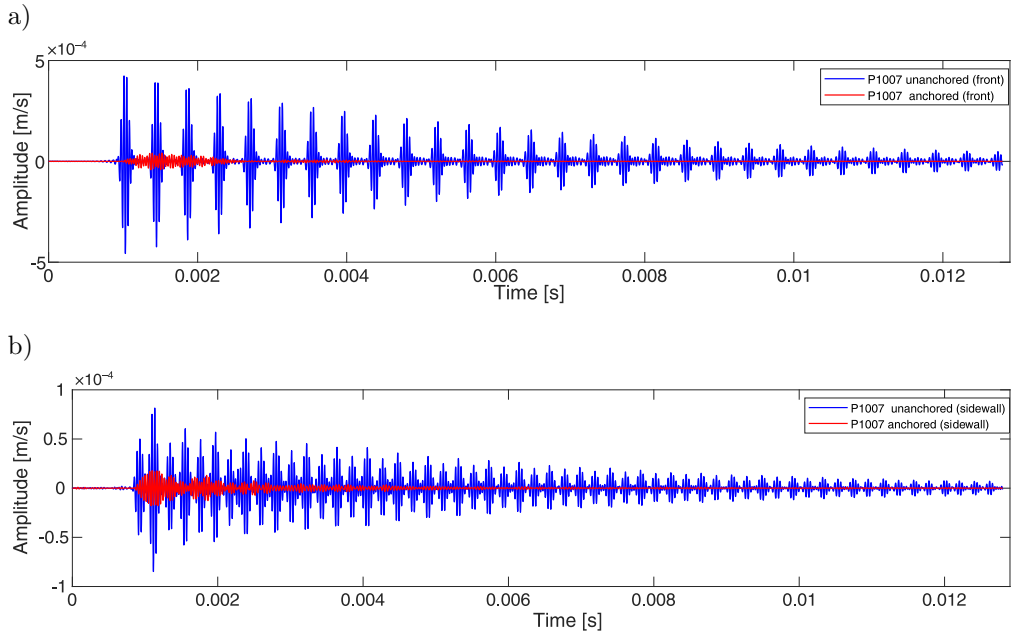


FIG. 11. Wave propagation in anchored (red signal) and unanchored (blue signal) bars:
a) wave measured from the front, b) wave measured on the sidewall.

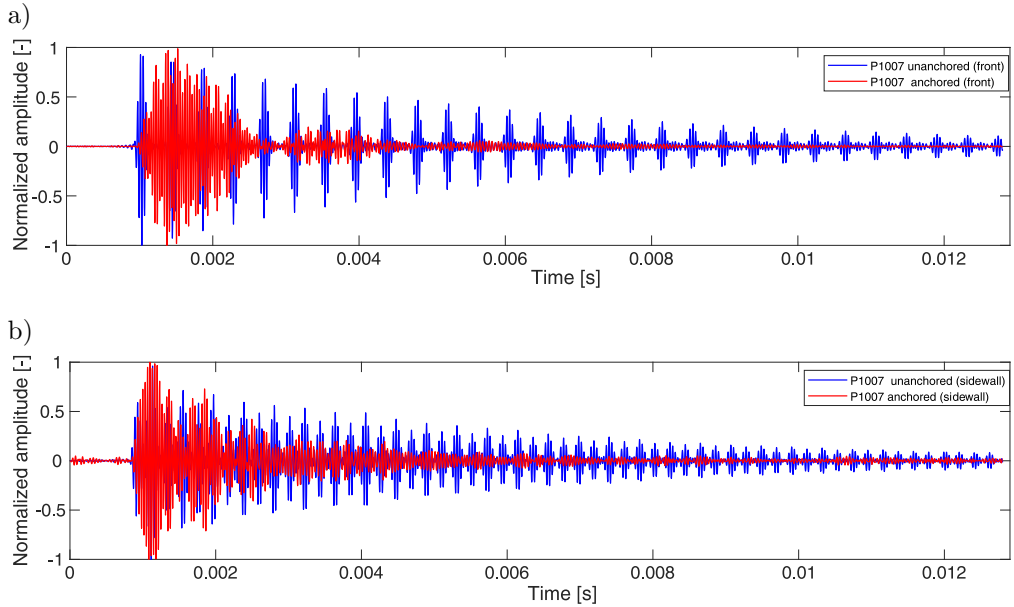


FIG. 12. Wave propagation in anchored and unanchored bars (normalized signal):
a) wave measured from the front, b) wave measured on the sidewall.

anchored bars in the standard machine at the final stage of examination. Furthermore, for future field applications, it is more practical to install PZT transducers rather than employ the LDV system (e.g., rods in a structure cannot be directly observed). Consequently, the signal was normalized, as shown in Fig. 12.

The differences in wave propagation between anchored and unanchored bars are evident, as shown in Fig. 12. These differences can be observed for both the waves recorded from the front and those recorded on the sidewall. Additionally, the wave recorded on the anchored bars does not separate into distinct wave packets as seen in the unanchored bars. Therefore, it is impossible to limit the analysis to the previously selected fragment (for unanchored bars) of the recorded wave. Instead, the signal registered on the anchored bars exhibits a more continuous nature. Due to anchoring on both ends, it is unclear from the signals where exactly the wave encounters the anchorage zone. Despite this, these results are promising for determining whether the rod has been anchored in a structure.

3.2.2. Verification of stress states. The verification of stress states in the material and their influence on wave propagation was carried out as part of the study. Rods with diameters of 10 mm and 16 mm were analyzed. Tensile tests were conducted using a testing machine, with waves recorded by PZT transducers (see Fig. 2d). The tests involved applying loads in increments of 10 kN, ranging from 0 to 70 kN for the 10 mm diameter rods, and from 0 to 150 kN for the 16 mm diameter rods. The recorded signals were analyzed in the time domain, focusing on parameters such as signal energy and the abscissa of the center of gravity of the signal square.

Figure 13 illustrates the variations in the propagation of the elastic wave for successive loads applied to the bar. As the load increases, the amplitude decreases. Furthermore, under the influence of the load, the signal shifts to the left. Based on this, we can conclude that the stress state in the element affects wave propagation.

To describe the changes in the signal, the following parameters were calculated using formulas (3.3) and (3.4) [24]:

– signal energy:

$$(3.3) \quad E_x = \sum_0^N x^2(n),$$

– abscissa of the center of gravity of the signal square:

$$(3.4) \quad \bar{n}_{x^2}^1 = \sum_0^N nx^2(n) \bigg/ \sum_0^N x^2(n),$$

where $x(n)$ represents the value of the signal at discrete time index n , and N represents the total number of registered signal samples.

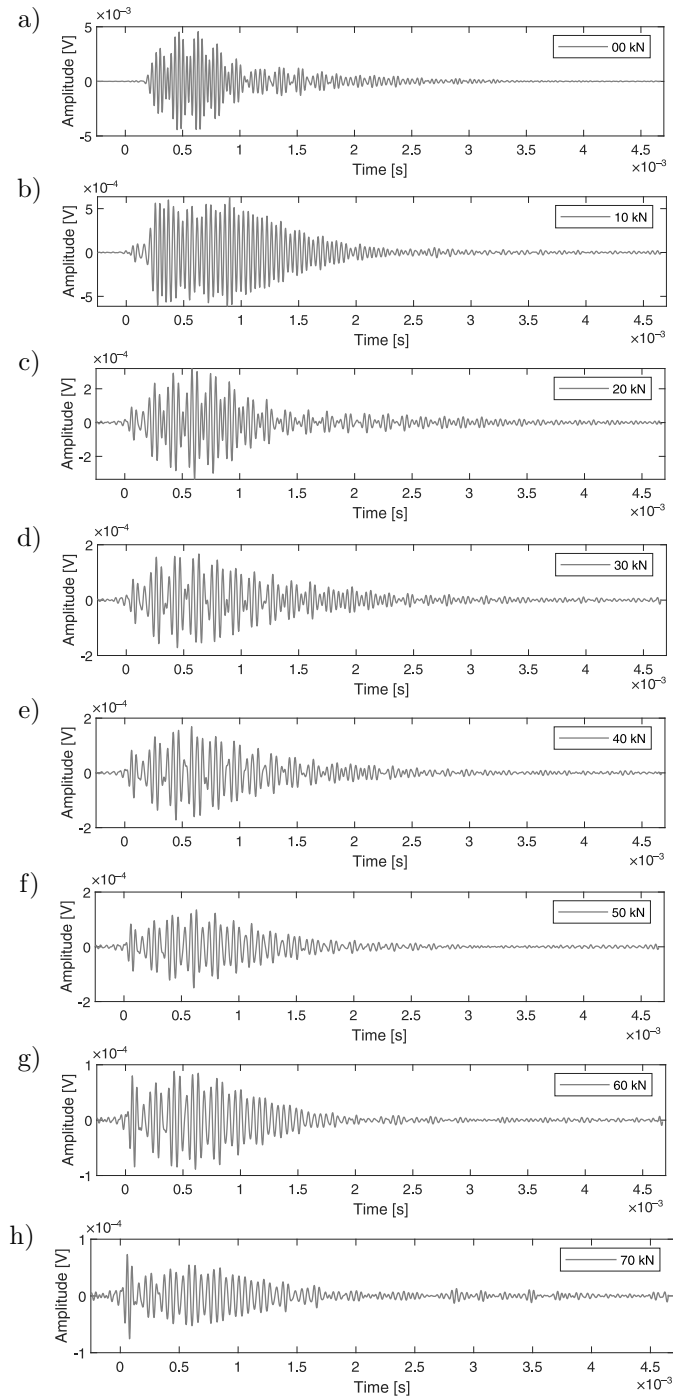


FIG. 13. Wave propagation depending on the applied force (sample P1006):
a) without load, b) 10 kN, c) 20 kN, d) 30 kN, e) 40 kN, f) 50 kN, g) 60 kN, h) 70 kN.

Due to differences noticeable at the beginning of the signal in Fig. 13, the signal energy and the abscissa of the center of gravity of the signal square were calculated over a restricted recording time interval (from 0 to $9e-4$ s). The comparison of signal energy for all 10 mm diameter samples is shown in Fig. 14a, while Fig. 14b displays the energy values over a narrower scope interval. The distribution of signal energy is illustrated in Fig. 14c. Figure 14d presents the distribution of signal energy for the 16 mm diameter samples. In Fig. 14a and 14b, the star symbol represents the experimental results of the signal energy calculated for specific force applied to the bar. The lines connecting these markers are used to visually depict the variation in signal energy as a function of force

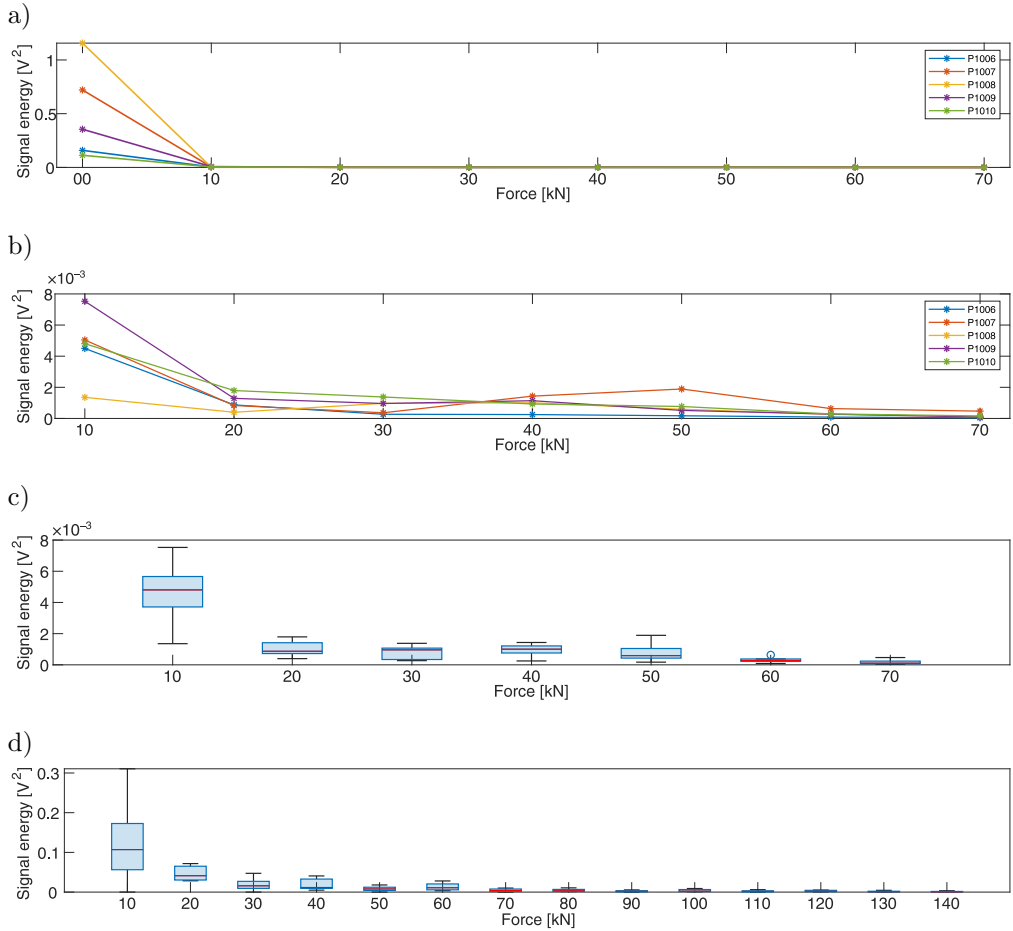


FIG. 14. a) Signal energy as a function of applied forces and its distribution (bars with a diameter of 10 mm); b) signal energy as a function of applied forces and its distribution in a narrowed range (bars with a diameter of 10 mm); c) distribution of signal energy in a narrowed range (bars with a diameter of 10 mm); d) distribution of signal energy in a narrowed range (bars with a diameter of 16 mm).

and do not represent measured values. Figure 14c shows the signal energy distribution for the 10 mm diameter bars under the same force level, while Fig. 14d presents the same for the 16 mm diameter bars. The edges of each box indicate the interquartile range, the middle red line within the box represents the median, and the lines extending beyond the box denote the range of results excluding outliers, which are shown as blue circles.

It can be observed that applying a load to the system causes a sharp decrease in signal energy. The significant drop in energy between 10 kN and 20 kN suggests considerable variability in signal behavior within this load range, as also observed in Figs. 13b and 13c (with decreases in amplitude values and changes in wave propagation). Successive increases in load values cause additional changes in energy levels (as the load level increases, the signal energy initially decreases, then slightly rises, and decreases again). Similar patterns in energy changes are observed across all samples, which may be useful for determining whether an element is subjected to a load. Similar results were also found for rods with a diameter of 16 mm. Moreover, comparing Figs. 14c and 14d reveals that the energy values for the 16 mm diameter rods are significantly higher than those for the 10 mm diameter rods. This may indicate that the larger volume of material allows for more efficient capture and propagation of elastic energy.

Figure 15 shows the signal in a narrowed time interval, with the abscissa of the signal's center of gravity marked for the unloaded state (Fig. 15a) and for the rod under maximum load (Fig. 15b).

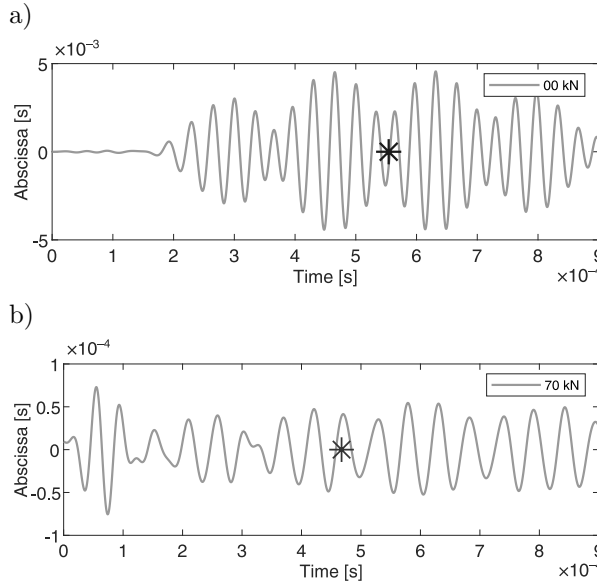


FIG. 15. Abscissa of the center of gravity of the signal square (sample P1006) corresponding to the load levels of: a) 0 kN, b) 70 kN.

As can be seen in Fig. 15, the abscissa is located in different places the two states. However, when comparing the abscissa for successive load increments across different samples no clear relationship emerges. It is challenging to pinpoint similar, clearly identified trends among different samples, regardless of bar diameter.

Considering the promising results for signal energy, the decision was made to divide the recorded signals into three equal time intervals: the first time interval from 0 to $3\text{e-}4$ s, the second from $3\text{e-}4$ s to $6\text{e-}4$ s, and the third from $6\text{e-}4$ s to $9\text{e-}4$ s. Signal energy was calculated for each interval, and the results are presented in a spatial plot (Fig. 16). Data points are color-coded according to the applied force level. Figure 16a presents results for the full load range (0–70 kN). As observed, the difference between the unloaded state and the first applied load is so large that the effect of subsequent loading cannot be seen. To address it, the load range was narrowed to 10–70 kN. Figure 16b shows the results for forces within this range. However, dense clustering near zero still prevents clear identification. Consequently, the range is further narrowed to 20–70 kN, as shown in Fig. 16c. In this plot, the differences corresponding to the successive load levels of the samples become more visible.

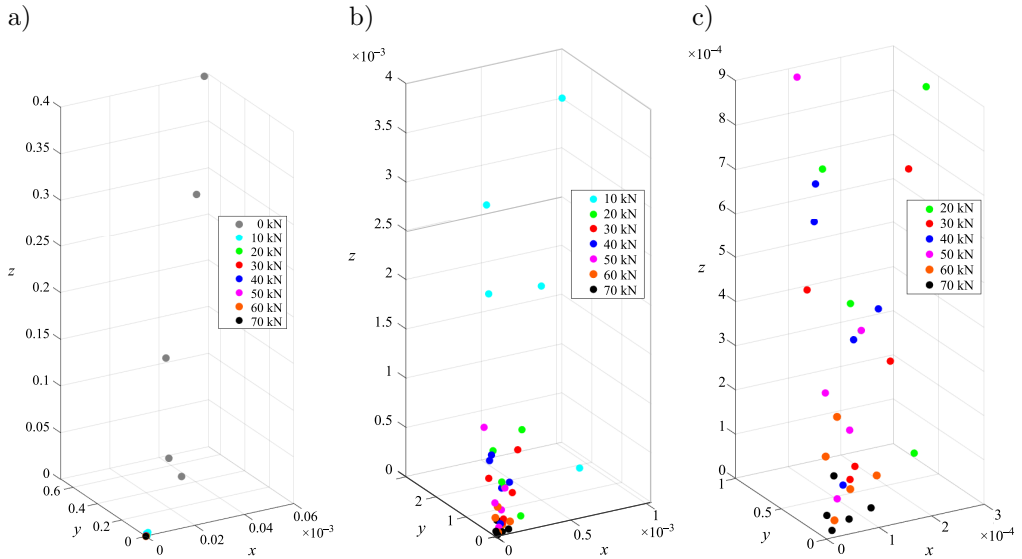


FIG. 16. Signal energy distribution across three time intervals for varying force levels, with the x , y , and z -axes representing energy from the 1st, 2nd, and 3rd intervals, respectively: a) force range from 0 kN to 70 kN, b) force range from 10 kN to 70 kN, c) force range from 20 kN to 70 kN.

For better visualization of the results, Fig. 17 shows views from three different perspectives: Fig. 17a shows the top view, Fig. 17b the left view, and

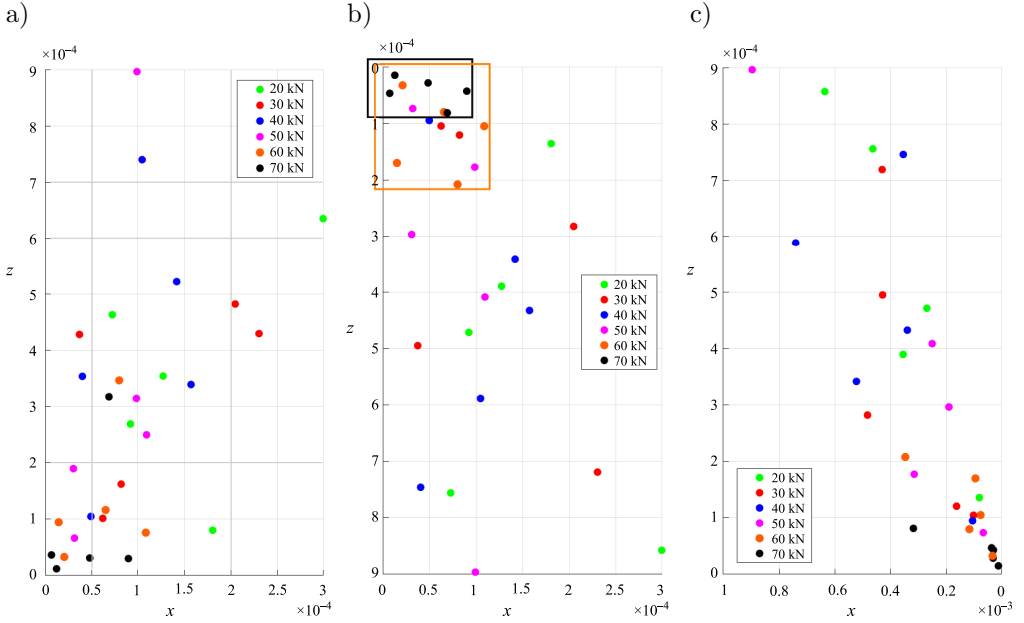


FIG. 17. Projections of signal energy distribution: a) 1st vs. 2nd interval energy, b) 1st vs. 3rd interval energy, c) 2nd vs. 3rd interval energy.

Fig. 17c the right view. Additionally, Fig. 17b highlights areas of result cumulation for forces of 60 kN and 70 kN. As can be observed in Figs. 16c and 17, the higher applied forces, the smaller differences in signal energy values in the selected time intervals for all samples studied. These outcomes are promising in terms of the potential determination of the bar's load level. To confirm this, expanding the database and conducting numerical simulations would be necessary.

3.2.3. Analysis of the destruction form. The final stage of the composite bar investigation involved analyzing the destruction proces. Due to non-uniform behavior of the samples during loading (as shown in Fig. 14b, where the signal energy for sample P1007 at 50 kN is different from that of other samples), the bars were underwent visual inspection after testing. Only the final failure patterns were evaluated and compared after removing the bars from the standard testing machine. Different damage mechanisms observed in bars with a diameter of 10 mm (samples P1006–P1010) are marked with colored ellipses in Fig. 18. The yellow ellipse indicates damage to the ribs of the bars, the green ellipse reveals protruding fibers in the anchorage zone, the blue one illustrates bar swelling (change in diameter), and the red ellipse indicates a complete detachment of the bar from the anchorage accompanied by fiber delamination. Although some

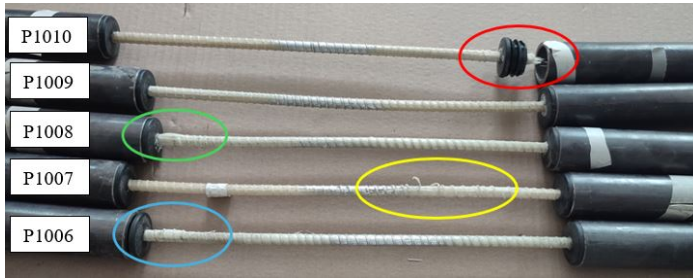


FIG. 18. Damaged reinforcement bars with a diameter of 10 mm (samples P1006–P1010).

damages were similar across sample (e.g., fiber cracking observed in samples P1007 and P1006), they did not occur in the same locations along the bar's length.

Similar damage patterns were observed in rods with a diameter of 16 mm, suggesting that the type of damage may be independent of the bar diameter. The application of artificial intelligence to predict failure mechanisms based on registered wave propagation signals is planned for future task.

4. SUMMARY AND CONCLUSION

This article presented the results of elastic wave propagation research on GFRP rods of different diameters. Measurements were conducted using laser Doppler vibrometry and piezoelectric transducers. The study focused on analyzing unanchored bars, the influence of anchoring, the influence of stress states, and the visual assessment of damage patterns.

The main conclusion drawn from the research are as follows:

- 1) Elastic waves measured from the front of the bar (opposite the excitation side) were more apparent, allowing for the extraction of regular, distinct wave packets. In contrast, those measured on the sidewall were denser and more compact.
- 2) In analyzed cases, differences in wave propagation caused by variations in specimen length was negligible during the initial part of the registered signal $\langle 0.0007 \text{ s}, 0.0017 \text{ s} \rangle$, corresponding to 2.5 wave cycles.
- 3) Rod diameter influences wave propagation – the larger the specimen diameter, the higher the value of experimentally determined wave velocity.
- 4) A satisfactory agreement between experimentally determined wave velocity and those calculated based on theoretical formulas was obtained.
- 5) Clear differences between anchored and unanchored bars were observed – identifying individual packets was difficult or even impossible in anchored rods.

- 6) The effect of the stress field in the rod on wave propagation was evident – the higher the applied force, the lower the energy of the registered signal.
- 7) The exact correlation between registered wave and the failure mode of the samples could not be definitively identified based on parameters such as signal energy or the abscissa of the center of gravity of the signal square. This may be due to the limited number of test samples. However, based on visual assessment, a few repeated defects can be pointed out: anchor rupture, rod swelling (diameter change), and fiber cracking.

The presented results are promising for a) determining the presence of anchorage and verifying material properties, b) identifying types of damage and accurately locating them, and c) identifying tensile forces in the rods based on guided wave analysis. However, it would be recommended to expand the database from experiments and numerical simulations to identify the most important features of wave propagation and deepen the understanding of these phenomena.

ACKNOWLEDGMENTS

This work was financed by the Minister of Science and Higher Education of the Republic of Poland under the program “Regional Excellence Initiative”.

DECLARATION OF CONFLICTING INTERESTS

The authors declare that there are no known competing financial interests or personal relationships that could have influence the work reported in this paper.

REFERENCES

1. SIWOWSKI T., *Bridges with FRP composites: Shaping, design, and testing* [in Polish: *Mosty z kompozytów FRP: Kształtowanie, projektowanie, badania*], WN PWN, Warsaw, 2018.
2. HASSANI S., MOUSAVI M., GANDOMI A.H., Structural health monitoring in composite structures: A comprehensive review, *Sensors*, **22**(1): 1234, 2022, <https://doi.org/10.3390/s22010153>.
3. CHEN J., YU Z., JIN H., Nondestructive testing and evaluation techniques of defects in fibre-reinforced polymer composites: A review, *Frontiers in Materials*, **9**: 567890, 2022 <https://doi.org/10.3389/fmats.2022.986645>.
4. WDOWIAK-POSTULAK A., ŚWIT G., DZIEDZIC-JAGOCKA I., Application of composite bars in wooden, full-scale, innovative engineering products – experimental and numerical study, *Materials*, **17**(3): 730, 2024, <https://doi.org/10.3390/ma17030730>.
5. SIWOWSKI T., KULPA M., RAJCHEL M., OBOZA D., Expansion of a bridge using FRP composite structures, *Nowoczesne Budownictwo Inżynieryjne*, **4**: 45–50, 2022.
6. QUARESHI J., A review of fibre reinforced polymer bridges, *Fibers*, **11**(5): 40, 2023, <https://doi.org/10.3390/fib11050040>.

7. GHOLIZADEH S., A review of non-destructive testing methods of composite materials, *Procedia Structural Integrity*, **1**: 42–50, 2016, <https://doi.org/10.1016/j.prostr.2016.02.008>.
8. JIAO P., EGBE K.J., NAZAR A.M., ALAVI A.H., Piezoelectric sensing techniques in structural health monitoring: A state-of-the-art review, *Sensors*, **20**(13): 3730, 2020, <https://doi.org/10.3390/s20133730>.
9. RADZIEJEWSKI M., KUDELA P., MARZANI A., DE MARCHI L., OSTACHOWICZ W., Damage identification in various types of composite plates using guided waves excited by a piezoelectric transducer and measured by a laser vibrometer, *Sensors*, **19**(9): 1958, 2019, <https://doi.org/10.3390/s19091958>.
10. ZHANG Y., JIA X., LIU Y., GAO E., SHUI L., Waves in elastic bars under axial constant velocity loading, *International Journal of Mechanical Sciences*, **273**: 109230, 2024, <https://doi.org/10.1016/j.ijmecsci.2024.109230>.
11. ZHANG X., WANG Q., Prediction of elastic wave propagation in composites using deep learning techniques, *SSRN Electronic Journal*, 2024, <https://doi.org/10.2139/ssrn.4546483>.
12. RIGBY S.E., BARR A.D., CLAYTON M., A review of Pochhammer-Chree dispersion in the Hopkinson bar. Review paper, *Proceedings of the Institution of Civil Engineers – Engineering and Computational Mechanics*, **171**: 1–21, 2017, <https://doi.org/10.1680/jencm.16.00027>.
13. CHREE C., The equations of an isotropic elastic solid in polar and cylindrical co-ordinates, their solution and application, *Transactions of the Cambridge Philosophical Society*, **14**: 250–369, 1887, <https://babel.hathitrust.org/cgi/pt?id=mdp.39015008919659&seq=276> (accessed on 2025.03.26).
14. HUANG G., SHI J., LIAN W., HONG L., ZHI S., YANG J., LIN C., ZHOU J., XIAO S., A sustainable steel-GFRP composite bars reinforced concrete structure: investigation of the bonding performance, *Buildings*, **14**(5): 1249, 2024, <https://doi.org/10.3390/buildings14051249>.
15. CHEN W., ZHEN H., LIU F., WU B., LI Z., WU Z., HUANG J., ZHU H., LI L., XIONG Z., Experimental and theoretical study on tensile mechanical properties of GFRP–steel composite bars, *Buildings*, **14**(8): 2513, 2024, <https://doi.org/10.3390/buildings14082513>.
16. RUCKA M., ZIMA B., Detection of rebar anchorage length using elastic wave propagation, *Journal of Civil Engineering, Environment and Architecture*, **31**(1): 67–80, 2014, <https://doi.org/10.7862/rb.2014.18>.
17. ALSUHAIBANI E., ALTURKI M., ALOGLA S.M., ALAWAD O., ALKHARISI M.K., BAYOUMI E., ALDUKAIL A., Compressive and bonding performance of GFRP-reinforced concrete columns, *Buildings*, **14**(4), 1071, 2024, <https://doi.org/10.3390/buildings14041071>.
18. Road and Bridge Research Institute, National Technical Assessment IBDiM-KOT-20211079, 2021.
19. WIATER A., SIWOWSKI T., Comparison of tensile properties of glass fibre reinforced polymer rebars by testing according to various standards, *Materials*, **13**(5): 1120, 2020, <https://doi.org/10.3390/ma13184110>.
20. ZIAJA D., JUREK M., An influence of actuator gluing on elastic wave excited in the structure, *Materials*, **17**(9): 2160, 2024, <https://doi.org/10.3390/ma17092160>.

21. ACHENBACH J.D., *Wave Propagation in Elastic Solids*, Center for Quality Engineering & Failure Prevention, Northwestern University, Evanston, IL 60208-3020, USA, Elsevier, 2018.
22. BANCROFT D., The velocity of longitudinal waves in cylindrical bars, *Physical Review*, **59**: 588, 1941, <https://doi.org/10.1103/PhysRev.59.588>.
23. AHMAD H., ELNEMR A., ALI N., HUSSAIN Q., CHAIYASARN K., JOYKLAD P., Finite element analysis of glass fiber-reinforced polymer-(GFRP) reinforced continuous concrete beams, *Polymers*, **13**(24): 4468, 2021, <https://doi.org/10.3390/polym13244468>.
24. ZIELIŃSKI T.P., *Digital Signal Processing: From Theory to Applications* [in Polish: *Cyfrowe przetwarzanie sygnałów: od teorii do zastosowań*], WKŁ, Warsaw, 2005.

Received December 20, 2024; accepted version April 8, 2025.

Online first July 10, 2025.
